Performance of an MEG Adaptive-Beamformer Source Reconstruction Technique in the Presence of Additive Low-Rank Interference

Kensuke Sekihara*, Srikantan S. Nagarajan, David Poeppel, and Alec Marantz

Abstract—**The influence of external interference on neuromagnetic source reconstruction by adaptive beamformer techniques was investigated. In our analysis, we assume that the interference has the following two properties: First, it is additive and uncorrelated with brain activity. Second, its temporal behavior can be characterized by a few distinct activities, and as a result, the spatio-temporal matrix of the interference has a few distinctly large singular values. Namely, the interference can be modeled as a low-rank signal. Under these assumptions, our analysis shows that the adaptive beamformer techniques are insensitive to interference when its spatial singular vectors are so different from a lead field vector of a brain source that the generalized cosine between these two vectors is much smaller than unity. Four types of numerical examples verifying this conclusion are presented.**

Index Terms—**Adaptive beamformer, biomagnetism, functional neuroimaging, magnetoencephalography, MEG inverse problems, neuromagnetic signal processing.**

I. Introduction

NEUROMAGNETIC measurements are often contaminated by various types of overlapping external interference even when the measurements are performed in a magnetically shielded room. Typical examples of such interference include magnetic noise from power lines or electric appliances such as elevators, automobiles or the subway. Small vibrations in neuromagnetometer hardware can cause large noises. Cardiac motions, muscle movements, or eye-blinks can also interfere with neuromagnetic measurements.

Recently developed external noise cancellation techniques [1] reduce such interference to some extent. However, when the interference is very large, a significant amount may still remain in the recordings. Also, external noise cancellation cannot work when the interference is sensor-channel specific, i.e., when it exists only in certain sensor recordings. This can happen, for example, when some sensors are particularly sensitive to a certain type of vibration but other sensors are not. When we estimate source distributions from magnetoencephalogram (MEG) measurements, the above-mentioned interferences generally cause severe errors in the final estimations.

A class of source estimation methods called adaptive beamformer techniques have attracted great interest. Adaptive-beamformer techniques were originally developed in the fields of array signal processing [2], and they have been successfully applied to neuromagnetic source reconstruction problems [3]–[7]. In this paper, we analyze the influence of external interference on the adaptive beamformer reconstruction results. Our analysis assumes the following properties: First, the interferences are additive and uncorrelated with brain signals. Second, the temporal behavior of the interference can be characterized by only a few distinct activities and, as a result, the covariance matrix of the interference has only a few distinctly large eigenvalues. Namely, the interference can be modeled as a low-rank signal.

Our analysis shows that adaptive beamformer techniques are insensitive to such interference when the eigenvectors of the covariance matrix are very different from the source lead field vectors. Since many types of interference with artificial (nonbiological) origins should have eigenvectors very different from the lead field of a brain source, we can conclude that the adaptive beamformer techniques are generally robust to the overlaps of such interference. In this paper, Section II briefly reviews adaptive-beamformer techniques for neuromagnetic reconstruction. Section III presents our theoretical analysis. Section IV presents the results of several numerical experiments that validate the arguments in Section III. Throughout this paper, plain italics indicate scalars, lower-case boldface italics indicate vectors, and upper-case boldface italics indicate matrices. The eigenvalues are numbered in decreasing order.

II. Adaptive-Beamformer Techniques for Neuromagnetic Reconstruction

A. Definitions

We define the magnetic field measured by the mth detector coil at time t as $b_m(t)$, and a column vector $\boldsymbol{b}(t) = [b_1(t), b_2(t), \ldots, b_M(t)]^T$ as a set of measured data where M is the total number of detector coils and superscript

Manuscript received January 20, 2003; revised May 11, 2003. The work of K. Sekihara was supported in part by Grants-in-Aid from the Kayamori Foundation of Informational Science Advancement, in part by Grants-in-Aid from Magnetic Health Science Foundation, and in part by the Ministry of Education, Science, Culture and Sports in Japan under Grant-in-Aid C13680948. The work of S. S. Nagarajan was supported in part by the Whitaker Foundation and in part by the National Institute of Health (NIH) under Grant P41RR12553-03 and Grant R01-DC004855-01A1. The work of D. Poeppel was supported in part by the National Institute of Health (NIH) under Grant NIH-R01-DC5660. Asterisk indicates corresponding author.

*K. Sekihara is with the Department of Electronic Systems and Engineering, Tokyo Metropolitan Institute of Technology, Asahigaoka 6-6, Hino, Tokyo 191-0065, Japan (e-mail: ksekiha@cc.tmit.ac.jp).

S. S. Nagarajan is with the Department of Radiology, University of California, San Francisco, San Francisco, CA 94143 USA.

D. Poeppel is with the Department of Linguistics and Biology, University of Maryland, College Park, MD 20742 USA.

A. Marantz is with the Department of Linguistics and Philosophy, Massachusetts Institute of Technology, Cambridge, MA 02139 USA.

Digital Object Identifier 10.1109/TBME.2003.820329

T indicates the matrix transpose. The spatial location is represented by a three-dimensional (3-D) vector $\boldsymbol{r}$: $\boldsymbol{r} = (x, y, z)$. The covariance matrix of the measurement is denoted as $\boldsymbol{R}$, i.e., $\boldsymbol{R} = \langle \boldsymbol{b}(t)\boldsymbol{b}^T(t)\rangle$. A total of Q discrete sources are assumed to generate the neuromagnetic field, and the locations of these sources are denoted as $\boldsymbol{r}_1, \boldsymbol{r}_2, \ldots, \boldsymbol{r}_Q$. The moment magnitude of the qth source is denoted as $s_q(t)$. The orientation of the qth source is defined as a 3-D vector $\boldsymbol{\eta}_q = [\eta_q^x, \eta_q^y, \eta_q^z]^T$ whose ζ component (where ζ equals x, y, or z) is equal to the cosine of the angle between the direction of the source moment and the ζ direction. We define $l_m^\zeta(\boldsymbol{r})$ as the output of the mth sensor. The output is induced by the unit-magnitude source located at $\boldsymbol{r}$ and directed in the ζ direction. The column vector $\boldsymbol{l}_\zeta(\boldsymbol{r})$ is defined as $\boldsymbol{l}_\zeta(\boldsymbol{r}) = [l_1^\zeta(\boldsymbol{r}), l_2^\zeta(\boldsymbol{r}), \cdots, l_M^\zeta(\boldsymbol{r})]^T$. The lead field matrix, which represents the sensitivity of the whole sensor array at $\boldsymbol{r}$, is defined as $\boldsymbol{L}(\boldsymbol{r}) = [\boldsymbol{l}_x(\boldsymbol{r}), \boldsymbol{l}_y(\boldsymbol{r}), \boldsymbol{l}_z(\boldsymbol{r})]$. The lead-field vector in the source-moment direction is defined as $\boldsymbol{l}(\boldsymbol{r}, \boldsymbol{\eta})$ where $\boldsymbol{l}(\boldsymbol{r}, \boldsymbol{\eta}) = \boldsymbol{L}(\boldsymbol{r})\boldsymbol{\eta}(\boldsymbol{r})$.

B. Adaptive-Beamformer Source Reconstruction

To solve neuromagnetic source reconstruction problems, we focus on the class of techniques referred to as the adaptive beamformer, which was originally developed in the field of array signal processing [2], [8]. One well-known adaptive beamformer is the minimum-variance beamformer [9], and two kinds of extensions have been proposed to incorporate the 3-D vector nature of sources in neuromagnetic reconstruction. One kind, called the scalar beamformer, uses the following formulation:

$$\widehat{s}(\boldsymbol{r}, t) = \boldsymbol{w}^T(\boldsymbol{r})\boldsymbol{b}(t) \tag{1}$$

where $\widehat{s}(\boldsymbol{r}, t)$ is the estimated source-moment time course obtained as the beamformer output. The weight $\boldsymbol{w}(\boldsymbol{r})$ is derived by minimizing $\boldsymbol{w}^T(\boldsymbol{r})\boldsymbol{R}\boldsymbol{w}(\boldsymbol{r})$ under the constraint that $\boldsymbol{l}^T(\boldsymbol{r}, \boldsymbol{\eta})\boldsymbol{w}(\boldsymbol{r}) = 1$. The explicit form of the scalar-type weight is known to be [3]

$$\boldsymbol{w}(\boldsymbol{r}) = \frac{\boldsymbol{R}^{-1}\boldsymbol{l}(\boldsymbol{r}, \boldsymbol{\eta})}{\boldsymbol{l}^T(\boldsymbol{r}, \boldsymbol{\eta})\boldsymbol{R}^{-1}\boldsymbol{l}(\boldsymbol{r}, \boldsymbol{\eta})}. \tag{2}$$

Note that the weight in (2) depends not only on the spatial location $\boldsymbol{r}$ but also on the orientation $\boldsymbol{\eta}$, and therefore, information regarding the source orientation is needed to calculate $\boldsymbol{w}(\boldsymbol{r})$. Using this weight, the time-averaged source power is obtained from [3]

$$\left\langle \widehat{s}(\boldsymbol{r}, t)^2 \right\rangle = \frac{1}{\boldsymbol{l}^T(\boldsymbol{r}, \boldsymbol{\eta})\boldsymbol{R}^{-1}\boldsymbol{l}(\boldsymbol{r}, \boldsymbol{\eta})}. \tag{3}$$

The other kind of extension, called the vector-type beamformer, enables the simultaneous estimation of the source orientation and source magnitude. It uses a set of three weight vectors, $\boldsymbol{w}_x(\boldsymbol{r})$, $\boldsymbol{w}_y(\boldsymbol{r})$, and $\boldsymbol{w}_z(\boldsymbol{r})$, each of which estimates the x, y, and z components of the source moment. A set of weights for a vector-extended minimum-variance beamformer is given by [10], [11]

$$[\boldsymbol{w}_x(\boldsymbol{r}), \boldsymbol{w}_y(\boldsymbol{r}), \boldsymbol{w}_z(\boldsymbol{r})] = \boldsymbol{R}^{-1}\boldsymbol{L}(\boldsymbol{r}) \left[\boldsymbol{L}^T\boldsymbol{R}^{-1}\boldsymbol{L}(\boldsymbol{r})\right]^{-1}. \tag{4}$$

The x, y, and z components of the source moment are estimated from

$$[\widehat{s}_x(\boldsymbol{r}, t), \widehat{s}_y(\boldsymbol{r}, t), \widehat{s}_z(\boldsymbol{r}, t)]^T = [\boldsymbol{w}_x(\boldsymbol{r}), \boldsymbol{w}_y(\boldsymbol{r}), \boldsymbol{w}_z(\boldsymbol{r})]^T \boldsymbol{b}(t) \tag{5}$$

where $\widehat{s}_\zeta(\boldsymbol{r}, t)$ is the estimated source moment in the ζ direction ($\zeta = x$, y, or z). The magnitude of the source moment is estimated from

$$\widehat{s}(\boldsymbol{r}, t) = \boldsymbol{w}_{\mathrm{opt}}^T(\boldsymbol{r})\boldsymbol{b}(t) \tag{6}$$

where $\boldsymbol{w}_{\mathrm{opt}}(\boldsymbol{r}) = [\boldsymbol{w}_x(\boldsymbol{r}), \boldsymbol{w}_y(\boldsymbol{r}), \boldsymbol{w}_z(\boldsymbol{r})]\widehat{\boldsymbol{\eta}}$, and $\widehat{\boldsymbol{\eta}}$ is the estimated source orientation obtained using (5). It can be shown that the weight $\boldsymbol{w}_{\mathrm{opt}}(\boldsymbol{r})$ is mathematically equivalent to the scalar beamformer weight in (2) with $\boldsymbol{\eta}$ giving the maximum beamformer outputs [12]. Therefore, in our following analysis, we use the scalar beamformer formulation for simplicity, but the results of the analysis are also valid for the weight $\boldsymbol{w}_{\mathrm{opt}}(\boldsymbol{r})$ obtained from the vector beamformer formulation.

III. Beamformer Performance When Additive Low-Rank Interference Exists

We denote the interference carried by the mth sensor channel at time t as $d_m(t)$. The column vector $\boldsymbol{d}(t) = [d_1(t), \ldots, d_M(t)]^T$ represents the interference contained in the measurements of the whole sensor array. We assume that $\boldsymbol{d}(t)$ is additive, so the measured data $\boldsymbol{b}(t)$ is expressed as

$$\boldsymbol{b}(t) = \sum_{q=1}^{Q} \boldsymbol{l}(\boldsymbol{r}_q, \boldsymbol{\eta}_q)s_q(t) + \boldsymbol{d}(t) + \boldsymbol{n}(t) = \boldsymbol{b}_s(t) + \boldsymbol{d}(t) \tag{7}$$

where

$$\boldsymbol{b}_s(t) = \sum_{q=1}^{Q} \boldsymbol{l}(\boldsymbol{r}_q, \boldsymbol{\eta}_q)s_q(t) + \boldsymbol{n}(t) \tag{8}$$

and $\boldsymbol{n}(t)$ is the sensor noise that can be modeled using a white Gaussian random process uncorrelated between sensor channels. The power of the sensor noise is denoted as σ_0^2, and it is assumed to be equal for all channels. We define the spatio-temporal matrix of the measurement $\boldsymbol{b}(t)$ as $\boldsymbol{B}$, such that $\boldsymbol{B} = [\boldsymbol{b}(t_1), \ldots, \boldsymbol{b}(t_K)]$. Here, $(t_1, \ldots, t_K)$ are the time points where the measurements are taken. The spatio-temporal matrix of the source signal plus noise, $\boldsymbol{b}_s(t)$, is defined as $\boldsymbol{B}_S$: $\boldsymbol{B}_S = [\boldsymbol{b}_s(t_1), \ldots, \boldsymbol{b}_s(t_K)]$, and the spatio-temporal matrix of the interference as $\boldsymbol{B}_d$: $\boldsymbol{B}_d = [\boldsymbol{d}(t_1), \ldots, \boldsymbol{d}(t_K)]$. Then, relationship $\boldsymbol{B} = \boldsymbol{B}_S + \boldsymbol{B}_d$ holds.

We next define the covariance matrix obtained from $\boldsymbol{b}_s(t)$, as $\boldsymbol{R}_b$, i.e., $\boldsymbol{R}_b = \langle \boldsymbol{b}_s(t)\boldsymbol{b}_s^T(t)\rangle$. We also define the covariance matrix of the interference as $\boldsymbol{R}_d$, i.e., $\boldsymbol{R}_d = \langle \boldsymbol{d}(t)\boldsymbol{d}^T(t)\rangle$. Assuming that interference $\boldsymbol{d}(t)$ is uncorrelated with $\boldsymbol{b}_s(t)$, we derive the relationship

$$\boldsymbol{R} = \boldsymbol{R}_b + \boldsymbol{R}_d \tag{9}$$

and from (1), the output of the beamformer is given by

$$[\widehat{s}(\boldsymbol{r}, t_1), \ldots, \widehat{s}(\boldsymbol{r}, t_K)] = \alpha \boldsymbol{l}^T\boldsymbol{R}^{-1}\boldsymbol{B} \tag{10}$$

where $\alpha = 1/[\boldsymbol{l}^T\boldsymbol{R}^{-1}\boldsymbol{l}]$. Here, we omit the explicit notations of $\boldsymbol{r}$ and $\boldsymbol{\eta}$ from the lead field vector for simplicity.

The key assumption for $\boldsymbol{R}_d$ in our analysis is that $\boldsymbol{R}_d$ is a low-rank matrix and has only a few distinctly large eigenvalues. That is, $\boldsymbol{R}_d$ can be expressed as

$$\boldsymbol{R}_d = \sum_{j=1}^{Q_D} \lambda_j \boldsymbol{u}_j \boldsymbol{u}_j^T \tag{11}$$

where λ_j and $\boldsymbol{u}_j$ are the jth eigenvalue of $\boldsymbol{R}_d$ and its corresponding eigenvector. Here, Q_D is the number of nonzero eigenvalues, and we assume that $Q_D \ll M$. In this case, using the singular value decomposition, the spatio-temporal matrix $\boldsymbol{B}_d$ is expressed as

$$\boldsymbol{B}_d = \sum_{j=1}^{Q_D} \sqrt{\lambda_j} \boldsymbol{u}_j \boldsymbol{v}_j^T \tag{12}$$

where $\boldsymbol{v}_j$ is the jth temporal singular vector of $\boldsymbol{B}_d$. We first analyze the simplest case where $\boldsymbol{R}_d$ is a rank-one matrix. In such cases, omitting the subscript for eigenvalue numbering, $\boldsymbol{R}_d$ is expressed as $\boldsymbol{R}_d = \lambda \boldsymbol{u}\boldsymbol{u}^T$. Then, we derive

$$\begin{aligned}\boldsymbol{R}^{-1} &= (\boldsymbol{R}_b + \lambda \boldsymbol{u}\boldsymbol{u}^T)^{-1} \\ &= \boldsymbol{R}_b^{-1} - \boldsymbol{R}_b^{-1} \frac{\boldsymbol{u}\boldsymbol{u}^T}{\frac{1}{\lambda} + \boldsymbol{u}^T \boldsymbol{R}_b^{-1} \boldsymbol{u}} \boldsymbol{R}_b^{-1} \\ &= \boldsymbol{R}_b^{-1} - \boldsymbol{R}_b^{-1} \frac{\boldsymbol{u}\boldsymbol{u}^T}{\boldsymbol{u}^T \boldsymbol{R}_b^{-1} \boldsymbol{u}} \boldsymbol{R}_b^{-1}\end{aligned} \tag{13}$$

where we use the relationship $1/\lambda \ll \boldsymbol{u}^T \boldsymbol{R}_b^{-1} \boldsymbol{u}$. Because $\boldsymbol{u}^T \boldsymbol{R}_b^{-1} \boldsymbol{u} \approx 1/\sigma_0^2$ (the proof is presented in Appendix) and the power of the interference is equal to λ, this relationship holds under the assumption that the power of the interference is much larger than the power of the sensor noise.

Substituting (13) and $\boldsymbol{B}_d = \sqrt{\lambda}\boldsymbol{u}\boldsymbol{v}^T$ into (10), we obtain

$$\begin{aligned}&[\widehat{s}(\boldsymbol{r}, t_1), \ldots, \widehat{s}(\boldsymbol{r}, t_K)] \\ &= \alpha \boldsymbol{l}^T \boldsymbol{R}_b^{-1} (\boldsymbol{B}_S + \sqrt{\lambda}\boldsymbol{u}\boldsymbol{v}^T) \\ &\quad - \alpha \frac{\left[\boldsymbol{l}^T \boldsymbol{R}_b^{-1} \boldsymbol{u}\right] \left[\boldsymbol{u}^T \boldsymbol{R}_b^{-1} (\boldsymbol{B}_S + \sqrt{\lambda}\boldsymbol{u}\boldsymbol{v}^T)\right]}{\boldsymbol{u}^T \boldsymbol{R}_b^{-1} \boldsymbol{u}} \\ &= \alpha \boldsymbol{l}^T \boldsymbol{R}_b^{-1} \boldsymbol{B}_S - \alpha \left[\frac{\boldsymbol{l}^T \boldsymbol{R}_b^{-1} \boldsymbol{u}}{\boldsymbol{u}^T \boldsymbol{R}_b^{-1} \boldsymbol{u}}\right] \boldsymbol{u}^T \boldsymbol{R}_b^{-1} \boldsymbol{B}_S \\ &= \alpha \widetilde{\boldsymbol{l}}^T \boldsymbol{R}_b^{-1} \boldsymbol{B}_S\end{aligned} \tag{14}$$

where

$$\widetilde{\boldsymbol{l}} = \boldsymbol{l} - \left[\frac{\boldsymbol{l}^T \boldsymbol{R}_b^{-1} \boldsymbol{u}}{\boldsymbol{u}^T \boldsymbol{R}_b^{-1} \boldsymbol{u}}\right] \boldsymbol{u}. \tag{15}$$

Using (13), the value of α is found to be

$$\frac{1}{\alpha} = \boldsymbol{l}^T \boldsymbol{R}^{-1} \boldsymbol{l} = \boldsymbol{l}^T \boldsymbol{R}_b^{-1} \boldsymbol{l} - \frac{\left[\boldsymbol{l}^T \boldsymbol{R}_b^{-1} \boldsymbol{u}\right]^2}{\boldsymbol{u}^T \boldsymbol{R}_b^{-1} \boldsymbol{u}} = \widetilde{\boldsymbol{l}}^T \boldsymbol{R}_b^{-1} \widetilde{\boldsymbol{l}}. \tag{16}$$

Therefore, substituting (16) into (14), we finally derive

$$\widehat{s}(\boldsymbol{r}, t) = \frac{\boldsymbol{l}^T \boldsymbol{R}^{-1} \boldsymbol{b}(t)}{\boldsymbol{l}^T \boldsymbol{R}^{-1} \boldsymbol{l}} = \frac{\widetilde{\boldsymbol{l}}^T \boldsymbol{R}_b^{-1} \boldsymbol{b}_s(t)}{\widetilde{\boldsymbol{l}}^T \boldsymbol{R}_b^{-1} \widetilde{\boldsymbol{l}}}. \tag{17}$$

The above equations indicate that the temporal behavior of the interference represented by the temporal singular vector $\boldsymbol{v}$ does not affect the beamformer output. These equations also indicate that the interference affects the output through its spatial singular vector $\boldsymbol{u}$ by modifying the lead field vector $\boldsymbol{l}$ into $\widetilde{\boldsymbol{l}}$ according to (15).

When the brain sources are well separated from each other, neglecting the sensor noise, the beamformer output at the qth source location is derived by replacing $\boldsymbol{b}_s(t)$ with $s_q(t)\boldsymbol{l}(\boldsymbol{r}_q, \boldsymbol{\eta}_q)$ in (17). Denoting $\boldsymbol{l}(\boldsymbol{r}_q, \boldsymbol{\eta}_q)$ as $\boldsymbol{f}$, the time course output is expressed as

$$\begin{aligned}\widehat{s}(\boldsymbol{r}, t) &= s_q(t) \frac{\widetilde{\boldsymbol{l}}^T \boldsymbol{R}_b^{-1} \boldsymbol{f}}{\widetilde{\boldsymbol{l}}^T \boldsymbol{R}_b^{-1} \widetilde{\boldsymbol{l}}} \\ &= s_q(t) \frac{\boldsymbol{l}^T \boldsymbol{R}_b^{-1} \boldsymbol{f}}{\boldsymbol{l}^T \boldsymbol{R}_b^{-1} \boldsymbol{l}} \\ &\quad \times \frac{\left[1 - \frac{\cos\left(\boldsymbol{l}, \boldsymbol{u} | \boldsymbol{R}_b^{-1}\right) \cos\left(\boldsymbol{f}, \boldsymbol{u} | \boldsymbol{R}_b^{-1}\right)}{\cos\left(\boldsymbol{l}, \boldsymbol{f} | \boldsymbol{R}_b^{-1}\right)}\right]}{\left[1 - \cos^2\left(\boldsymbol{l}, \boldsymbol{u} | \boldsymbol{R}_b^{-1}\right)\right]}\end{aligned} \tag{18}$$

and its power output is given by

$$\left\langle \widehat{s}(\boldsymbol{r}, t)^2 \right\rangle = \frac{1}{\widetilde{\boldsymbol{l}}^T \boldsymbol{R}_b^{-1} \widetilde{\boldsymbol{l}}} = \frac{1}{\boldsymbol{l}^T \boldsymbol{R}_b^{-1} \boldsymbol{l} \left[1 - \cos^2\left(\boldsymbol{l}, \boldsymbol{u} | \boldsymbol{R}_b^{-1}\right)\right]}. \tag{19}$$

In the above equations, the generalized cosine with the metric $\boldsymbol{A}^{-1}$ between two column vectors $\boldsymbol{a}_1$ and $\boldsymbol{a}_2$ is defined as

$$\cos^2(\boldsymbol{a}_1, \boldsymbol{a}_2 | \boldsymbol{A}^{-1}) = \frac{\left[\boldsymbol{a}_1^T \boldsymbol{A}^{-1} \boldsymbol{a}_2\right]^2}{\left[\boldsymbol{a}_1^T \boldsymbol{A}^{-1} \boldsymbol{a}_1\right] \left[\boldsymbol{a}_2^T \boldsymbol{A}^{-1} \boldsymbol{a}_2\right]}. \tag{20}$$

Because the definition of the generalized cosine is very similar to the correlation coefficient, the generalized cosine can quantify the similarity or the difference of the two vectors. Thus, when any lead field vector in the source space is very different from the spatial eigenvector of the interference $\boldsymbol{u}$, the relationships $\cos^2(\boldsymbol{l}, \boldsymbol{u} | \boldsymbol{R}_b^{-1}) \ll 1$ and $\cos^2(\boldsymbol{f}, \boldsymbol{u} | \boldsymbol{R}_b^{-1}) \ll 1$ hold. When these relationships hold, (18) and (19) can be changed to

$$\widehat{s}(\boldsymbol{r}, t) \approx s_q(t) \frac{\boldsymbol{l}^T \boldsymbol{R}_b^{-1} \boldsymbol{f}}{\boldsymbol{l}^T \boldsymbol{R}_b^{-1} \boldsymbol{l}} = \frac{\boldsymbol{l}^T \boldsymbol{R}_b^{-1} \boldsymbol{b}_s(t)}{\boldsymbol{l}^T \boldsymbol{R}_b^{-1} \boldsymbol{l}} \tag{21}$$

and

$$\left\langle \widehat{s}(\boldsymbol{r}, t)^2 \right\rangle \approx \frac{1}{\boldsymbol{l}^T \boldsymbol{R}_b^{-1} \boldsymbol{l}}. \tag{22}$$

These equations clearly indicate that influence of the interference is negligible in such cases.

So far, our analysis assumes that $\boldsymbol{R}_d$ is a rank-one matrix. The analysis can be extended to the case where $\boldsymbol{R}_d$ is a rank-two matrix. In this case, $\boldsymbol{R}_d$ and $\boldsymbol{B}_d$ are expressed as $\boldsymbol{R}_d = \lambda_1 \boldsymbol{u}_1 \boldsymbol{u}_1^T + \lambda_2 \boldsymbol{u}_2 \boldsymbol{u}_2^T$ and $\boldsymbol{B}_d = \sqrt{\lambda_1}\boldsymbol{u}_1 \boldsymbol{v}_1^T + \sqrt{\lambda_2}\boldsymbol{u}_2 \boldsymbol{v}_2^T$. Substituting these equations into (10) and assuming the relationships

$$\frac{\left(\boldsymbol{u}_1^T \boldsymbol{R}_b^{-1} \boldsymbol{u}_2\right)}{\left(\boldsymbol{u}_1^T \boldsymbol{R}_b^{-1} \boldsymbol{u}_1\right)} \approx 0 \quad \text{and} \quad \frac{\left(\boldsymbol{u}_1^T \boldsymbol{R}_b^{-1} \boldsymbol{u}_2\right)}{\left(\boldsymbol{u}_2^T \boldsymbol{R}_b^{-1} \boldsymbol{u}_2\right)} \approx 0 \tag{23}$$

after lengthy calculations, we finally get

$$\widehat{s}(\boldsymbol{r}, t) = \frac{\boldsymbol{l}^T \boldsymbol{R}_b^{-1} \boldsymbol{b}(t)}{\boldsymbol{l}^T \boldsymbol{R}_b^{-1} \boldsymbol{l}} = \frac{\widetilde{\boldsymbol{l}}^T \boldsymbol{R}_b^{-1} \boldsymbol{b}_s(t)}{\widetilde{\boldsymbol{l}}^T \boldsymbol{R}_b^{-1} \widetilde{\boldsymbol{l}}} \tag{24}$$

where

$$\widetilde{\boldsymbol{l}} = \boldsymbol{l} - \left[\frac{\boldsymbol{l}^T \boldsymbol{R}_b^{-1}\boldsymbol{u}_1}{\boldsymbol{u}_1^T \boldsymbol{R}_b^{-1}\boldsymbol{u}_1}\right]\boldsymbol{u}_1 - \left[\frac{\boldsymbol{l}^T \boldsymbol{R}_b^{-1}\boldsymbol{u}_2}{\boldsymbol{u}_2^T \boldsymbol{R}_b^{-1}\boldsymbol{u}_2}\right]\boldsymbol{u}_2. \tag{25}$$

We can then derive (26) and (27) as shown at the bottom of page. These equations show that the second eigenvector $\boldsymbol{u}_2$ affects the beamformer outputs in an additive manner and, therefore, the influence from this eigenvector is negligible if $\cos(\boldsymbol{l}, \boldsymbol{u}_2|\boldsymbol{R}_b^{-1}) \ll 1$. The analysis can be further extended to the general case where the rank of $\boldsymbol{R}_d$ is equal to Q_D, and it can be shown that each eigenvector influences the beamformer outputs in exactly the same additive manner.

IV. Numerical Experiments

A series of numerical experiments were conducted to check the validity of the analysis in Section III. A sensor alignment of the 148-sensor array from Magnes 2500 (4D Neuroimaging Inc., San Diego, CA) neuromagnetometer was used. The coordinate origin was set at the center of the sensor coil located at the center of the coil array. The x direction was defined as that from posterior to anterior, the y direction was defined as that from the right to the left hemisphere, and z direction was defined as that perpendicular to the surface of the coil at the origin. Three point sources were assumed to exist on a plane defined as $x = 1.0$. (The values of the spatial coordinates (x, y, z) are expressed in centimeters.) The source-sensor configuration and the coordinate system are illustrated in Fig. 1.

The simulated magnetic recordings were calculated in the following manner. We denote the locations and orientations of the three sources as $\boldsymbol{r}_j$ and $\boldsymbol{\eta}_j$ ($j = 1, 2, 3$), which are listed in Table I. The lead field vectors of the three sources, $\boldsymbol{l}(\boldsymbol{r}_j, \boldsymbol{\eta}_j)$, were calculated ($j = 1, 2, 3$) by using the spherically homogeneous conductor model [13] with its center set at $(1, 0, -11)$. We then calculated the simulated magnetic-field recordings such that $\boldsymbol{b}_s(t) = \sum_j^3 s_j(t)\boldsymbol{l}(\boldsymbol{r}_j, \boldsymbol{\eta}_j) + \boldsymbol{n}(t)$, where the time courses $s_1(t)$, $s_2(t)$, and $s_3(t)$ were calculated by using

$$s_j(t) = \exp\left[\frac{(t-t_1)^2}{\Omega^2}\right]\sin\left[2\pi f(t - t_\theta)\right]$$
$$\text{for} \quad j = 1, 2, \quad \text{and}$$
$$s_3(t) = \sin\left[2\pi f(t - t_\theta)\right]. \tag{28}$$

In the above equations, Ω, t_1, f, and t_θ are the numerical parameters controlling the shapes of the time courses, and their values are listed in Table II. The three time courses are shown in Fig. 2(a). The magnetic-field recordings were calculated

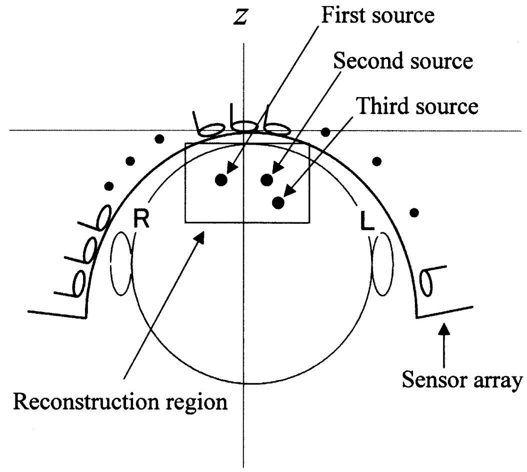

Fig. 1. The coordinate system and source-sensor configuration used in the numerical experiments. The coordinate origin was set at the center of the sensor coil located at the center of the array. The plane at $x = 1.0$ cm is shown. The large circle shows the cross section of the sphere used for the forward calculation, and the square shows the reconstruction region used for the results in Figs. 2(c) and 6.

TABLE I
Source Parameter Values Used for the Numerical Experiments in Section IV

source number	location (cm)	orientation
1	(1.0, –1.0, –6.0)	(1.0, 0., 0.)
2	(1.0, 1.0, –6.0)	(0.7, 0.7, 0.)
3	(1.0, 1.6, –7.2)	(0, 0.7, 0.7)

TABLE II
Values of the Parameters Used for Calculating $s_1(t)$, $s_2(t)$, and $s_3(t)$

s_j (t) (ms)	Ω (ms)	t_1 (ms)	f (Hz)	t_θ (ms)
$j = 1$	67.8	219	4.75	139
$j = 2$	105.3	246	7.6	123
$j = 3$	–	–	11.4	100

$$\widehat{s}(\boldsymbol{r}, t) = s_q(t)\frac{\boldsymbol{l}^T\boldsymbol{R}_b^{-1}\boldsymbol{f}}{\boldsymbol{l}^T\boldsymbol{R}_b^{-1}\boldsymbol{l}}\frac{\left[1 - \frac{\cos(\boldsymbol{l},\boldsymbol{u}_1|\boldsymbol{R}_b^{-1})\cos(\boldsymbol{f},\boldsymbol{u}_1|\boldsymbol{R}_b^{-1})}{\cos(\boldsymbol{l},\boldsymbol{f}|\boldsymbol{R}_b^{-1})} - \frac{\cos(\boldsymbol{l},\boldsymbol{u}_2|\boldsymbol{R}_b^{-1})\cos(\boldsymbol{f},\boldsymbol{u}_2|\boldsymbol{R}_b^{-1})}{\cos(\boldsymbol{l},\boldsymbol{f}|\boldsymbol{R}_b^{-1})}\right]}{\left[1 - \cos^2\left(\boldsymbol{l}, \boldsymbol{u}_1|\boldsymbol{R}_b^{-1}\right) - \cos^2\left(\boldsymbol{l}, \boldsymbol{u}_2|\boldsymbol{R}_b^{-1}\right)\right]} \tag{26}$$

and

$$\left\langle \widehat{s}(\boldsymbol{r}, t)^2 \right\rangle = \frac{1}{\boldsymbol{l}^T\boldsymbol{R}^{-1}\boldsymbol{l}}\frac{1}{\left[1 - \cos^2\left(\boldsymbol{l}, \boldsymbol{u}_1|\boldsymbol{R}_b^{-1}\right) - \cos^2\left(\boldsymbol{l}, \boldsymbol{u}_2|\boldsymbol{R}_b^{-1}\right)\right]} \tag{27}$$

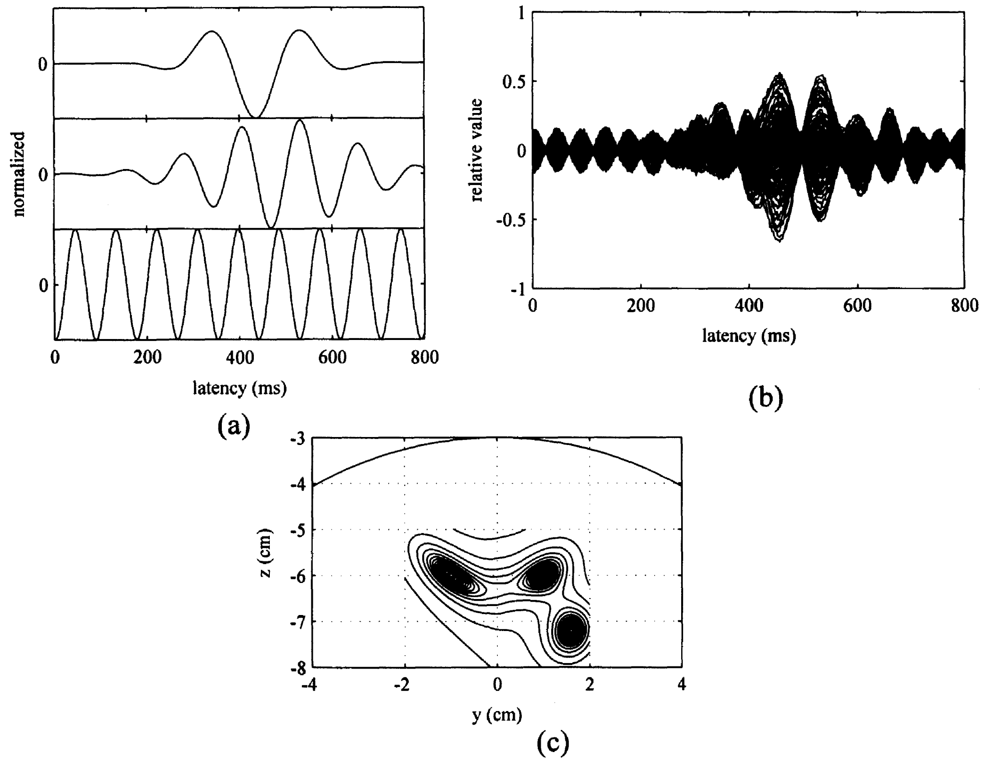

Fig. 2. (a) Time courses $s_1(t)$, $s_2(t)$, and $s_3(t)$ (from top to bottom) used for the numerical experiments. (b) The simulated magnetic-field recordings, which were calculated at 2-ms intervals from zero to 800 ms. White Gaussian noise was added in order for the SNR to equal eight. (c) The average power reconstruction $\sqrt{\langle \hat{s}(\boldsymbol{r},t)^2\rangle}$ obtained using the simulated magnetic field recordings in (b).

at 2-ms intervals from zero to 800 ms. The amplitude of the white Gaussian noise $\boldsymbol{n}(t)$ was set so that the resulting signal-to-noise ratio (SNR) was eight where the SNR is defined as $\sqrt{\langle\|\boldsymbol{b}_s(t)\|^2\rangle/\langle\|\boldsymbol{n}(t)\|^2\rangle}$ and $\langle\cdot\rangle$ indicates the time average over 800 ms. The simulated magnetic-field recordings are shown in Fig. 2(b). The source reconstruction was performed using (3). In the reconstruction, the covariance matrix $\boldsymbol{R}_b$ was calculated using $\boldsymbol{R}_b = \sigma_0^2\boldsymbol{I} + \sum_j^3\langle s_j(t)^2\rangle\boldsymbol{l}(\boldsymbol{r}_j,\boldsymbol{\eta}_j)\boldsymbol{l}^T(\boldsymbol{r}_j,\boldsymbol{\eta}_j)$. The results of source-power reconstruction obtained with this $\boldsymbol{R}_b$ are shown in Fig. 2(c), which shows the reconstruction when no interference exists.

In our numerical experiments, four types of interference $\boldsymbol{d}(t)$ were simulated. The first was the periodic interference where the interference for the jth sensor recording, $d_j(t)$, was calculated using $d_j(t) \propto \sin(2\pi f_d t + \phi)$ for 60 sensors over the right hemisphere and $d_j(t) = 0$ for other sensors. The frequency of this periodic interference f_d was set at 13.7 Hz, which is very close to the 10 Hz-frequency of the third source. The interference $\boldsymbol{d}(t)$ was then added to the signal magnetic field $\boldsymbol{b}_s(t)$ to generate simulated magnetic-field recordings $\boldsymbol{b}(t)$: $\boldsymbol{b}(t) = \boldsymbol{b}_s(t) + \boldsymbol{d}(t)$. The resultant simulated recordings are shown in Fig. 3(a).

The second type of interference was the same periodic interference except that the phase offset varies from sensor to sensor. That is, the interference $d_j(t)$ for the 60 sensors over the right hemisphere was calculated using $d_j(t) \propto \sin(2\pi f_d t + \phi_j)$ where each sensor had a different ϕ_j that was determined by generating the uniform random number between 0 and 2π. The simulated recordings containing this interference are shown in Fig. 3(b). It should be pointed out that it is difficult in practice to filter out such periodic interference as that in Fig. 3(a)–(b), because the frequency of the interference is very close to the frequencies of the signal source activities.

The third type of interference was a linear trend whose inclination varies from channel to channel. That is, d_j was calculated using $d_j = \Delta_j t$ where each sensor had a different value of Δ_j. The parameter Δ_j was determined by generating the Gaussian random number whose standard deviation was equal to $b_s^{max} \times 10^{-3}$, where b_s^{max} is the maximum value of $\|\boldsymbol{b}_s(t_k)\|/M$. Simulated recordings containing such a linear trend are shown in Fig. 3(c). The fourth type of interference was a combination of this linear trend with a low-frequency noise. In this case, $d_j(t)$ was calculated by using $d_j(t) = \Delta_j t + (b_s^{max}/2)\sin[2\pi f_d t + \phi]$ where f_d was set at 1.1 Hz and ϕ is the same for all sensor recordings. The simulated recordings containing this interference are shown in Fig. 3(d). It should again be pointed out that it is in practice difficult to filter out such low-frequency interference because actual MEG signals contain large amounts of low-frequency components.

The covariance matrix of interference $\boldsymbol{R}_d$ was calculated numerically using $\boldsymbol{R}_d = \langle\boldsymbol{d}(t)\boldsymbol{d}^T(t)\rangle$, and the total covariance matrix $\boldsymbol{R}$ was obtained using $\boldsymbol{R} = \boldsymbol{R}_b + \boldsymbol{R}_d$. The eigenvalue spectra of $\boldsymbol{R}_d$ for these four types of interference are shown in Fig. 4. The spectra show that the first and the third interferences have a single large eigenvalue, indicating that these interferences are rank-one interferences. The second and the

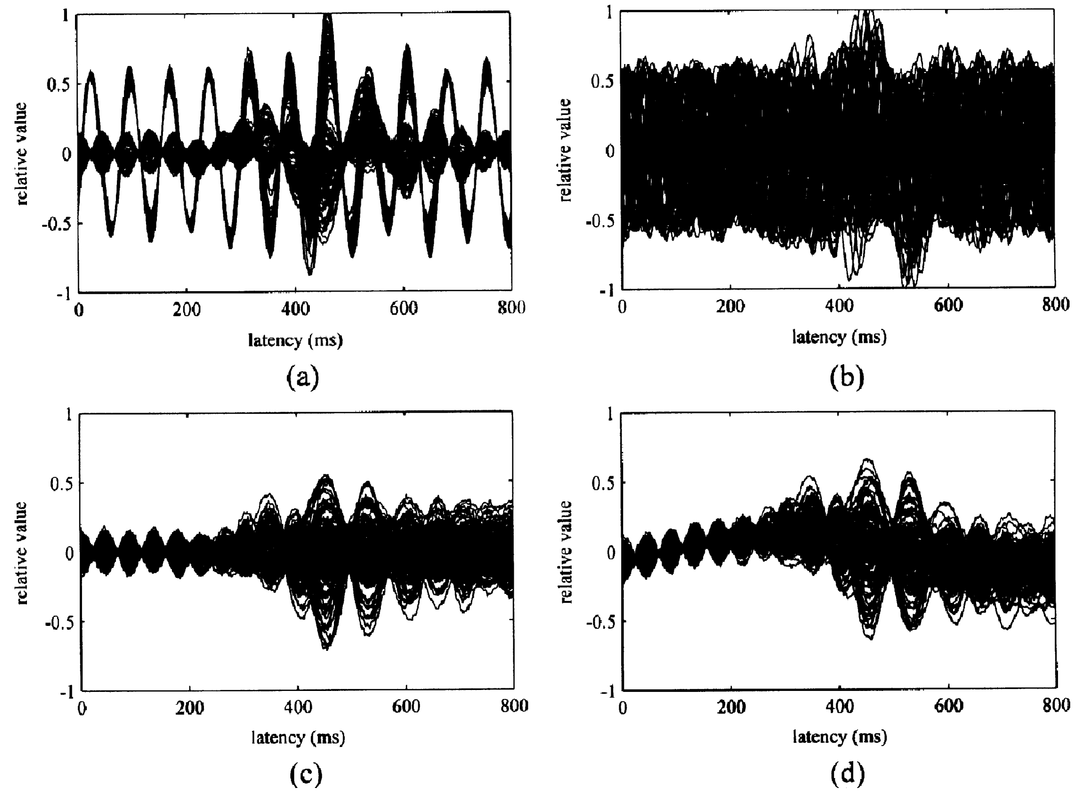

Fig. 3. Simulated magnetic-field recordings containing low-rank interferences. (a) A periodic interference with a frequency of 13.7 Hz was superimposed onto the recordings of 60 sensors located over the right hemisphere. (b) The same periodic noise, except that the phase offset varying from sensor to sensor, was superimposed onto the 60-sensor recordings over the right hemisphere. (c) A linear trend with its inclination varying from sensor to sensor was superimposed onto all sensor recordings. (d) A combination of the linear trend in (c) with a low-frequency noise of 1.1 Hz was superimposed onto all sensor recordings.

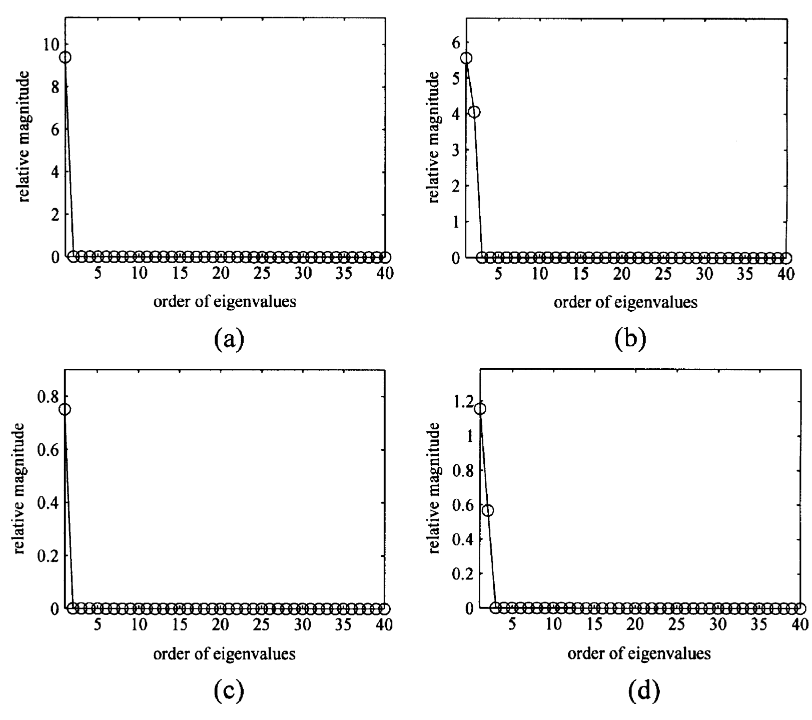

Fig. 4. Eigenvalue spectrum of $\boldsymbol{R}_d$ shown up to the 40th eigenvalue. (a) The periodic interference in Fig. 3(a). (b) The periodic interference with a random phase offset in Fig. 3(b). (c) The linear trend in Fig. 3(c). (d) The linear trend with a low-frequency noise of 1.1 Hz in Fig. 3(d).

fourth interferences have two distinctly large eigenvalues, indicating that they are rank-two interferences. The contour plots of the first spatial eigenvectors of the four kinds of interferences are shown in Fig. 5(b)–(e). The lead field vector of the second source is also shown in Fig. 5(a) as a typical lead field from a brain source.

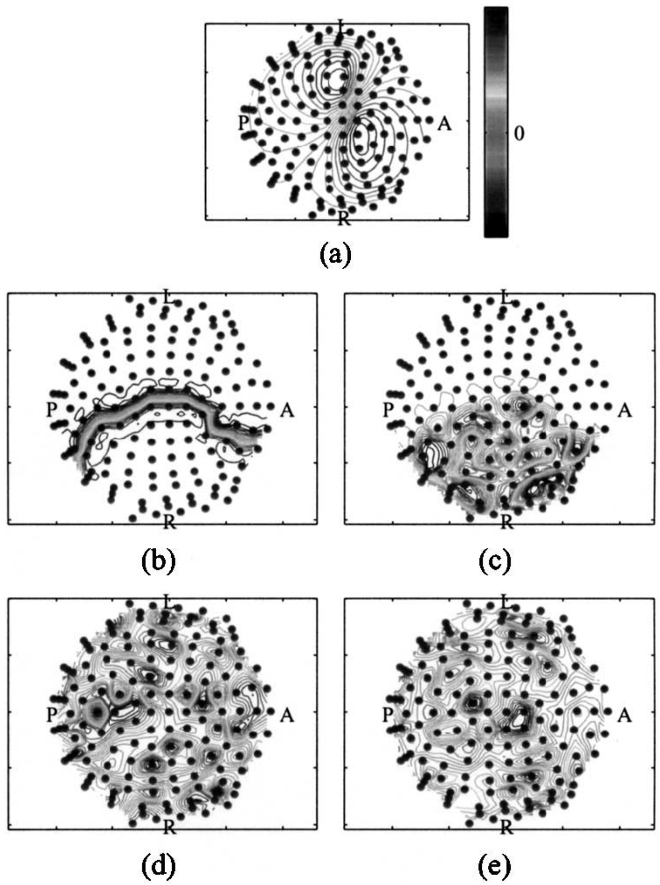

Fig. 5. (a) The contour plot of the lead field vector for the second source, $\boldsymbol{l}(\boldsymbol{r}_2, \boldsymbol{\eta}_2)$. (b) The contour plots of the first eigenvector of $\boldsymbol{R}_d$. The periodic interference shown in Fig. 3(a) was applied. (c) The first eigenvector of $\boldsymbol{R}_d$. The periodic interference with a random phase offset shown in Fig. 3(b) was applied. (d) The first eigenvector of $\boldsymbol{R}_d$. The linear trend shown in Fig. 3(c) was applied. (e) The first eigenvector of $\boldsymbol{R}_d$. The linear trend with a low-frequency noise of 1.1 Hz shown in Fig. 3(d) was applied. The dots represent locations of sensors. (The locations are slightly distorted.) The anterior, posterior, left and right directions are indicated by A, P, L, and R, respectively.

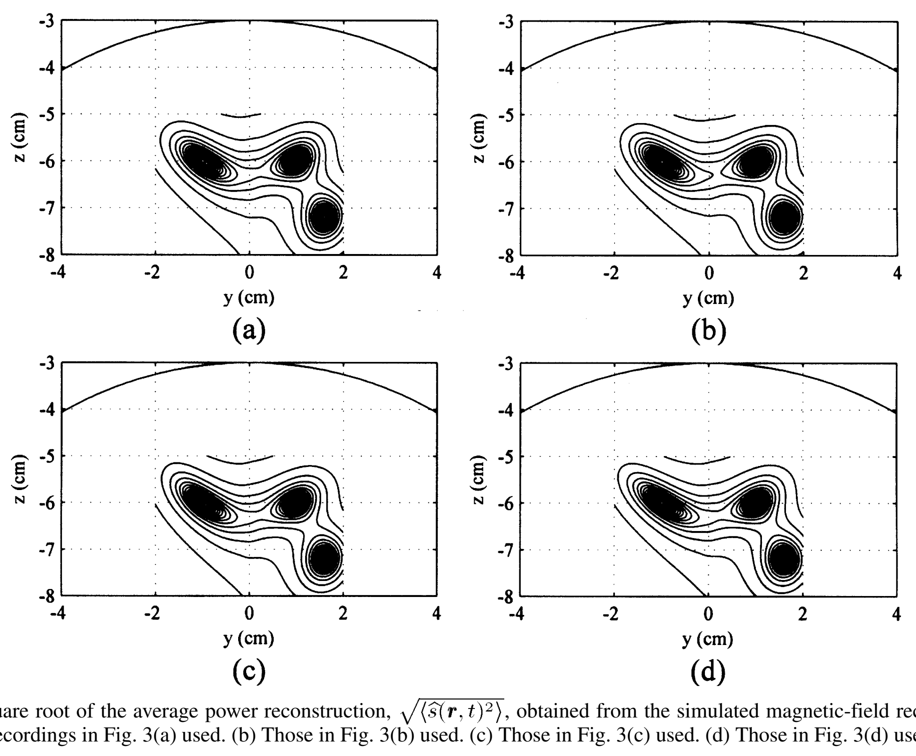

Fig. 6. Results of the square root of the average power reconstruction, $\sqrt{\langle \widehat{s}(\boldsymbol{r},t)^2 \rangle}$, obtained from the simulated magnetic-field recordings in Fig. 3. (a) The simulated magnetic-field recordings in Fig. 3(a) used. (b) Those in Fig. 3(b) used. (c) Those in Fig. 3(c) used. (d) Those in Fig. 3(d) used. The reconstruction was performed by using (3).

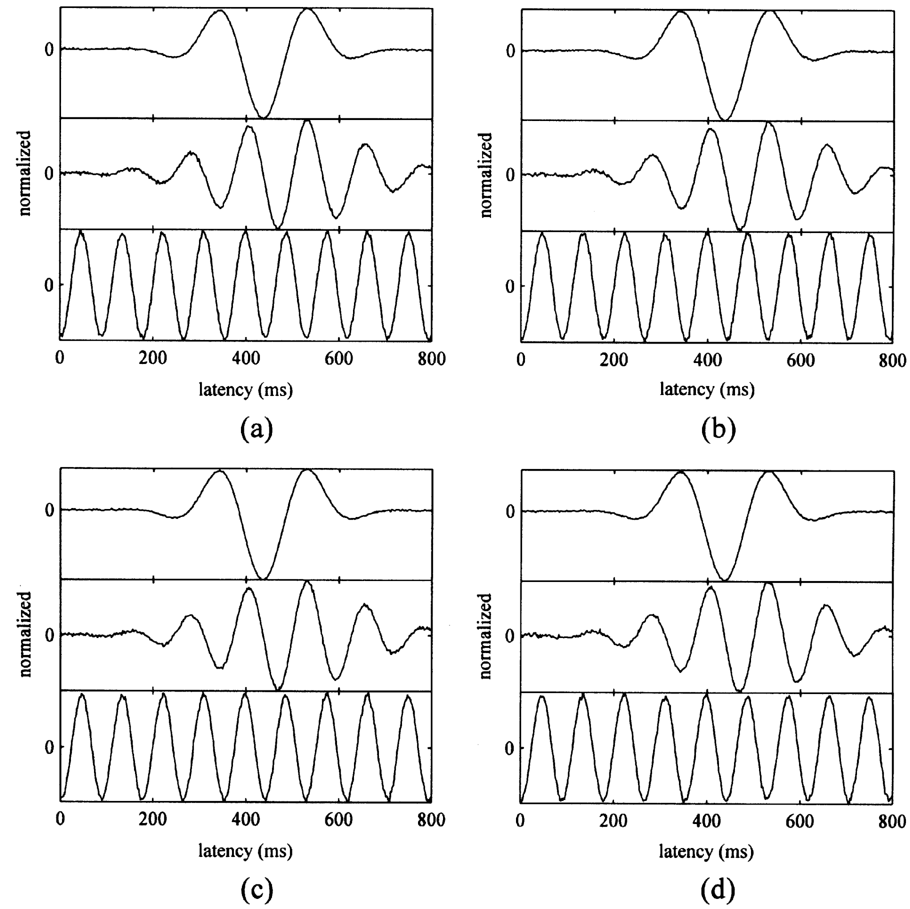

Fig. 7. The source time-course estimates $\widehat{s}(\boldsymbol{r}_j, t)$ (where $j = 1$, 2, and 3) obtained from the simulated magnetic-field recordings in Fig. 3. (a) The simulated magnetic-field recordings in Fig. 3(a) used. (b) Those in Fig. 3(b) used. (c) Those in Fig. 3(c) used. (d) Those in Fig. 3(d) used. The reconstruction was performed by using (1) and (2).

It can be seen that the spatial eigenvectors for all four cases are very different from this lead field. The values of the generalized cosine $\cos^2(\boldsymbol{l}, \boldsymbol{u}|\boldsymbol{R}_b^{-1})$ are less than 3×10^{-3} for all four cases. These very small values of the generalized cosine confirm our visually obtained interpretation that the eigenvectors in Fig. 5 are very different from the lead field vector of a brain source. The value of $(\boldsymbol{u}_1^T \boldsymbol{R}_b^{-1} \boldsymbol{u}_2)/(\boldsymbol{u}_1^T \boldsymbol{R}_b^{-1} \boldsymbol{u}_1)$ was also calculated for the rank-two interferences. This value was on the order of 10^{-6} for these cases. The generalized cosine between the lead field vector and the second eigenvector was less than 3×10^{-3} for the cases in Fig. 3(b)–(d). These numerical evaluations suggest that the influence of the interferences should be very small, according to our analysis in Section III. The beamformer reconstruction was applied to the four cases in Fig. 3. The results of source power reconstruction are shown in Fig. 6. The source-activity time courses are shown in Fig. 7. No observable influence exists in any of the results in Figs. 6 and 7. In the results shown in Fig. 7, the correlation coefficients between the reconstructed and the original time courses were found to be greater than 0.99 for all the three time courses in any of the four cases. These results clearly demonstrate the validity of our analysis in Section III.

V. Discussion

In deriving (14), we assume that the power of the interference is much larger than the power of the sensor noise. Because the power of the interference is equal to λ and $\boldsymbol{u}^T \boldsymbol{R}_b^{-1} \boldsymbol{u}$ is approximately equal to $1/\sigma_0^2$ (as shown in Appendix), this assumption leads to the condition $1/\lambda \ll \boldsymbol{u}^T \boldsymbol{R}_b^{-1} \boldsymbol{u}$. When the power of the interference is comparable to the power of the sensor noise, this condition is not satisfied and (14) should be changed to

$$[\widehat{s}(\boldsymbol{r}, t_1), \ldots, \widehat{s}(\boldsymbol{r}, t_K)] = \alpha \widetilde{\boldsymbol{l}}^T \boldsymbol{R}_b^{-1} \boldsymbol{B}_S + \frac{\sqrt{\lambda}}{1 + \frac{\lambda}{\sigma_0^2}} \alpha \left[\boldsymbol{l}^T \boldsymbol{R}_b^{-1} \boldsymbol{u}\right] \boldsymbol{v}^T. \tag{29}$$

The second term of the right-hand side of the above equation represents the time course of the interference contained in the beamformer output. The amplitude of this interference time course is proportional to $\alpha[\boldsymbol{l}^T \boldsymbol{R}_b^{-1} \boldsymbol{u}]$.

To evaluate the amplitude, we consider a simple case where a single source exists. Its lead field vector and its power are denoted as $\boldsymbol{f}$ and σ_1^2, respectively. Assuming that the beamformer is exactly tuned to this source, i.e., $\boldsymbol{l} = \boldsymbol{f}$, we can derive

$$\frac{\sqrt{\lambda}}{1 + \frac{\lambda}{\sigma_0^2}} \alpha \left[\boldsymbol{l}^T \boldsymbol{R}_b^{-1} \boldsymbol{u}\right] \boldsymbol{v}^T = \frac{\sqrt{\lambda}}{1 + \frac{\lambda}{\sigma_0^2}} \cdot \frac{\cos(\boldsymbol{f}, \boldsymbol{u})}{\|\boldsymbol{f}\| \left[1 - \zeta \cos^2(\boldsymbol{f}, \boldsymbol{u})\right]} \boldsymbol{v}^T \tag{30}$$

where $\zeta = \lambda/[(\lambda+\sigma_0^2)(1+\rho)]$ and $\rho = (\sigma_1^2/\sigma_0^2)\|\boldsymbol{f}\|^2$. Therefore, when the lead field vector of a brain source is so different from $\boldsymbol{u}$ that the relationship $\cos(\boldsymbol{f},\boldsymbol{u}) \approx 0$ holds, the amplitude of the interference time course in the beamformer output is nearly equal to zero. This conclusion can be extended to a case where multiple sources exist and to a case where no source exists.

Because the square of the weight norm $\|\boldsymbol{w}(\boldsymbol{r})\|^2$ is the white-noise power gain in the beamformer reconstruction process, the quantity $\langle \widehat{s}(\boldsymbol{r},t)^2\rangle/\|\boldsymbol{w}(\boldsymbol{r})\|^2$ is approximately proportional to the SNR in the beamformer output. This quantity, defined as $\mathcal{Z}$, is sometimes used for evaluating the statistical significance of the reconstructed results [3]. The $\mathcal{Z}$ value is expressed as

$$\mathcal{Z} = \frac{\langle \widehat{s}(\boldsymbol{r},t)^2\rangle}{\|\boldsymbol{w}(\boldsymbol{r})\|^2} = \frac{\boldsymbol{l}^T(\boldsymbol{r},\boldsymbol{\eta})\boldsymbol{R}^{-1}\boldsymbol{l}(\boldsymbol{r},\boldsymbol{\eta})}{\boldsymbol{l}^T(\boldsymbol{r},\boldsymbol{\eta})\boldsymbol{R}^{-2}\boldsymbol{l}(\boldsymbol{r},\boldsymbol{\eta})}. \tag{31}$$

In a manner similar to deriving (16), we can derive

$$\begin{aligned}\mathcal{Z} &= \frac{\boldsymbol{l}^T(\boldsymbol{r},\boldsymbol{\eta})\boldsymbol{R}^{-1}\boldsymbol{l}(\boldsymbol{r},\boldsymbol{\eta})}{\boldsymbol{l}^T(\boldsymbol{r},\boldsymbol{\eta})\boldsymbol{R}^{-2}\boldsymbol{l}(\boldsymbol{r},\boldsymbol{\eta})}\\ &= \frac{\boldsymbol{l}^T(\boldsymbol{r},\boldsymbol{\eta})\boldsymbol{R}_b^{-1}\boldsymbol{l}(\boldsymbol{r},\boldsymbol{\eta})}{\boldsymbol{l}^T(\boldsymbol{r},\boldsymbol{\eta})\boldsymbol{R}_b^{-2}\boldsymbol{l}(\boldsymbol{r},\boldsymbol{\eta})}\frac{\left[1-\cos^2\left(\boldsymbol{l},\boldsymbol{u}|\boldsymbol{R}_b^{-1}\right)\right]}{(1-\nu)}\end{aligned} \tag{32}$$

where

$$\nu = \frac{\boldsymbol{l}^T\boldsymbol{R}_b^{-1}\boldsymbol{u}}{\boldsymbol{u}^T\boldsymbol{R}_b^{-1}\boldsymbol{u}}\left[2\frac{\boldsymbol{l}^T\boldsymbol{R}_b^{-2}\boldsymbol{u}}{\boldsymbol{l}^T\boldsymbol{R}_b^{-2}\boldsymbol{l}} - \left(\frac{\boldsymbol{l}^T\boldsymbol{R}_b^{-1}\boldsymbol{u}}{\boldsymbol{u}^T\boldsymbol{R}_b^{-1}\boldsymbol{u}}\right)\left(\frac{\boldsymbol{u}^T\boldsymbol{R}_b^{-2}\boldsymbol{u}}{\boldsymbol{l}^T\boldsymbol{R}_b^{-2}\boldsymbol{l}}\right)\right]. \tag{33}$$

Therefore, when the assumptions that $\cos^2(\boldsymbol{l},\boldsymbol{u}|\boldsymbol{R}_b^{-1}) \ll 1$ and $|\nu| \ll 1$ hold, the influence of the interference on the $\mathcal{Z}$ value is also negligible. The value ν is small when $\boldsymbol{l}$ and $\boldsymbol{u}$ are very different because only the numerators in (33) contain the cross products of $\boldsymbol{l}$ and $\boldsymbol{u}$. In the numerical experiments in Section IV, ν is always less than 10^{-6} for all four interference cases.

The minimum-variance beamformer is known to be very sensitive to errors in the forward modeling or errors in estimating the measurement covariance matrix [14]. The eigenspace-projection beamformer provides an output SNR higher than that of the minimum-variance beamformer when such errors exist [15]. Redefining the weight vector obtained from (2) as $\boldsymbol{w}^{(\mathrm{MV})}$, the extension to the eigenspace-projection beamformer is defined as [15]

$$\boldsymbol{w}(\boldsymbol{r}) = \boldsymbol{E}_S\boldsymbol{E}_S^T\boldsymbol{w}^{(\mathrm{MV})}(\boldsymbol{r}) \tag{34}$$

where $\boldsymbol{E}_S$ is a matrix whose column vectors are the eigenvectors of $\boldsymbol{R}$ that correspond to the eigenvalues from the signal (and interference). Therefore, using (10), the output of the eigenspace-projection beamformer is given by

$$\begin{aligned}&[\widehat{s}(\boldsymbol{r},t_1),\ldots,\widehat{s}(\boldsymbol{r},t_K)]\\ &= \left[\boldsymbol{E}_S\boldsymbol{E}_S^T\boldsymbol{w}^{(\mathrm{MV})}(\boldsymbol{r})\right]^T\boldsymbol{B}\\ &= \alpha\boldsymbol{l}^T\boldsymbol{R}_b^{-1}\boldsymbol{E}_S\boldsymbol{E}_S^T(\boldsymbol{B}_s+\sqrt{\lambda}\boldsymbol{u}\boldsymbol{v}^T).\end{aligned} \tag{35}$$

Since the source lead field vector $\boldsymbol{l}(\boldsymbol{r}_q,\boldsymbol{\eta}_q)$ and the eigenvector $\boldsymbol{u}$ exist in the signal-plus-interference subspace, they are unaffected by the signal-plus-interference-subspace projector $\boldsymbol{E}_S\boldsymbol{E}_S^T$, i.e.,

$$\boldsymbol{E}_S\boldsymbol{E}_S^T(\boldsymbol{B}_S+\sqrt{\lambda}\boldsymbol{u}\boldsymbol{v}^T) = \boldsymbol{B}_S+\sqrt{\lambda}\boldsymbol{u}\boldsymbol{v}^T. \tag{36}$$

Therefore, the same discussion as that for (14) can be applied to this case, leading to the conclusion that the time course estimate $\widehat{s}_q(t)$ from the eigenspace-projected beamformer is not affected by the interference $\boldsymbol{d}(t)$.

In summary, we analyzed the influences of additive low-rank interference on the reconstruction results of MEG adaptive beamformer techniques. We found that the influence is negligible when the eigenvectors of the covariance matrix obtained from such interference are very different from any of the lead field vectors in the source space. The results of our numerical experiments confirmed this conclusion. The assumptions that interference is low rank and its spatial eigenvectors are different from the lead field of a brain source are generally satisfied for many types of artificial (nonbiological) interference, and the adaptive beamformer techniques are generally robust to the overlaps of such interference.

These assumptions, however, may not hold for some interference with biological origins. Several investigations have pointed out the possibility that background cortical activities are caused by a large number of randomly activated sources [16], [17]. Also, some biological interference such as that caused by eye blinks or cardiac motions may invalidate the assumption that $\cos^2(\boldsymbol{l},\boldsymbol{u}|\boldsymbol{R}_b^{-1}) \ll 1$ because the lead fields for an eye blink source or a cardiac source may not be very different from the lead field for a brain source. Therefore, the analysis presented in this paper cannot generally apply to interference with biological origins. Thus, methods should be developed to reduce the influence of such interference, with the possible application of preprocessing with independent-component-analysis techniques toward these ends [18].

APPENDIX

This appendix derives the relationship $\boldsymbol{u}^T\boldsymbol{R}_b^{-1}\boldsymbol{u} \approx 1/\sigma_0^2$. The assumption to derive it is that any lead field vector in the source space is so different from the spatial eigenvector of the interference $\boldsymbol{u}$ that their generalized cosine is approximately equal to zero. We first consider a simplest case where a single source exist whose lead field vector and the power are, respectively, denoted as $\boldsymbol{f}$ and σ_1^2. Then, $\boldsymbol{R}_b$ is expressed as $\boldsymbol{R}_b = \sigma_0^2\boldsymbol{I}+\sigma_1^2\boldsymbol{f}\boldsymbol{f}^T$ and $\boldsymbol{R}_b^{-1}$ is expressed as

$$\boldsymbol{R}_b^{-1} = \frac{1}{\sigma_0^2}\left[\boldsymbol{I} - \frac{\rho}{1+\rho}\cdot\frac{\boldsymbol{f}\boldsymbol{f}^T}{\|\boldsymbol{f}\|^2}\right]$$

where $\rho = (\sigma_1^2/\sigma_0^2)\|\boldsymbol{f}\|^2$. Thus, using $\cos^2(\boldsymbol{f},\boldsymbol{u}) \approx 0$, we derive

$$\boldsymbol{u}^T\boldsymbol{R}_b^{-1}\boldsymbol{u} = \frac{1}{\sigma_0^2}\left[1 - \frac{\rho}{1+\rho}\cdot\cos^2(\boldsymbol{f},\boldsymbol{u})\right] \approx \frac{1}{\sigma_0^2}. \tag{37}$$

When two sources exist, the power and the lead field vector of the second source are denoted as $\boldsymbol{g}$ and σ_2^2, and a matrix $\boldsymbol{D}$ is defined as $\sigma_0^2\boldsymbol{D} = \sigma_0^2\boldsymbol{I}+\sigma_1^2\boldsymbol{f}\boldsymbol{f}^T$. Here, because $\sigma_0^2\boldsymbol{D}$ is equal to the covariance matrix for the single-source case presented above, the relationship $\boldsymbol{u}^T\boldsymbol{D}^{-1}\boldsymbol{u} \approx 1$ holds. We define $\widetilde{\rho}$ as $\widetilde{\rho} = (\sigma_2^2/\sigma_0^2)\boldsymbol{g}^T\boldsymbol{D}^{-1}\boldsymbol{g}$. Using $\boldsymbol{u}^T\boldsymbol{D}^{-1}\boldsymbol{u} \approx 1$ and $\cos^2(\boldsymbol{u},\boldsymbol{g}|\boldsymbol{D}^{-1}) \approx 0$, we can finally derive

$$\boldsymbol{u}^T\boldsymbol{R}_b^{-1}\boldsymbol{u} = \frac{\boldsymbol{u}^T\boldsymbol{D}^{-1}\boldsymbol{u}}{\sigma_0^2}\left[1 - \frac{\widetilde{\rho}}{1+\widetilde{\rho}}\cdot\cos^2(\boldsymbol{u},\boldsymbol{g}|\boldsymbol{D}^{-1})\right] \approx \frac{1}{\sigma_0^2}. \tag{38}$$

It can be shown that the argument presented above is extended to a case where more than two sources exist.

ACKNOWLEDGMENT

The authors wish to thank Dr. S. Robinson and J. Vrba for their insightful discussions.

REFERENCES

[1] J. Vrba and S. Robinson *et al.*, "The effect of environmental noise on magnetometer- and gardiometer-based MEG systems," in *Proc. 12th Int. Conf. Biomagnetism*, R. Hari *et al.*, Eds: Helsinki Univ. Technol., 2001, pp. 953–956.

[2] B. D. van Veen and K. M. Buckley, "Beamforming: a versatile approach to spatial filtering," *IEEE Acoust. Speech, Audio Processing Mag.*, vol. 5, pp. 4–24, Apr. 1988.

[3] S. E. Robinson and J. Vrba *et al.*, "Functional neuroimaging by synthetic aperture magnetometry (SAM)," in *Recent Advances in Biomagnetism*, T. Yoshimoto *et al.*, Eds. Sendai, Japan: Tohoku Univ. Press, 1999, pp. 302–305.

[4] J. Gross and A. A. Ioannides, "Linear transformations of data space in MEG," *Phys. Med. Biol.*, vol. 44, pp. 2081–2097, 1999.

[5] K. Sekihara, S. S. Nagarajan, D. Poeppel, A. Marantz, and Y. Miyashita, "Reconstructing spatio-temporal activities of neural sources using an MEG vector beamformer technique," *IEEE Trans. Biomed. Eng.*, vol. 48, pp. 760–771, July 2001.

[6] I. Hashimoto, T. Kimura, Y. Iguchi, R. Takino, and K. Sekihara, "Dynamic activation of distinct cytoarchitectonic areas of the human SI cortex after median nerve stimulation," *NeuroReport*, vol. 12, pp. 1891–1897, 2001.

[7] I. Hashimoto, K. Sakuma, T. Kimura, Y. Iguchi, and K. Sekihara, "Serial activation of distinct cytoarchitectonic areas of the human SI cortex after posterior tibial nerve stimulation," *NeuroReport*, vol. 12, pp. 1857–1862, 2001.

[8] D. H. Johnson and D. E. Dudgeon, *Array Signal Processing: Concepts and Techniques*. Englewood Cliffs, NJ: Prentice-Hall, 1993.

[9] J. Capon, "High-resolution frequency wavenumber spectrum analysis," *Proc. IEEE*, vol. 57, pp. 1408–1419, 1969.

[10] M. E. Spencer, R. M. Leahy, J. C. Mosher, and P. S. Lewis, "Adaptive filters for monitoring localized brain activity from surface potential time series," in *Conf. Rec. 26th Annu. Asilomer Conf. Signals, Systems, and Computers*, Nov. 1992, pp. 156–161.

[11] B. D. van Veen, W. van Drongelen, M. Yuchtman, and A. Suzuki, "Localization of brain electrical activity via linearly constrained minimum variance spatial filtering," *IEEE Trans. Biomed. Eng.*, vol. 44, pp. 867–880, Sept. 1997.

[12] K. Sekihara, S. S. Nagarajan, D. Poeppel, and A. Marantz, "Asymptotic SNR of scalar and vector minimum-variance beamformers for neuromagnetic source reconstruction," *IEEE Trans. Biomed. Eng.*, submitted for publication.

[13] J. Sarvas, "Basic mathematical and electromagnetic concepts of the biomagnetic inverse problem," *Phys. Med. Biol.*, vol. 32, pp. 11–22, 1987.

[14] H. Cox, R. M. Zeskind, and M. M. Owen, "Robust adaptive beamforming," *IEEE Trans. Signal Processing*, vol. SP–35, pp. 1365–1376, 1987.

[15] K. Sekihara, S. S. Nagarajan, D. Poeppel, A. Marantz, and Y. Miyashita, "Application of an MEG eigenspace beamformer to reconstructing spatio-temporal activities of neural sources," *Human Brain Mapping*, vol. 15, pp. 199–215, 2002.

[16] J. C. de Munck, P. C. M. Vijn, and F. H. Lopes da Silva, "A random dipole model for spontaneous brain activity," *IEEE Trans. Biomed. Eng.*, vol. 39, pp. 791–804, Aug. 1992.

[17] B. Lütkenhöner, "Magnetic field arising from current dipoles randomly distributed in a homogeneous spherical volume conductor," *J. Appl. Phys.*, vol. 75, pp. 7204–7210, 1994.

[18] T. H. Sander, G. Wubbeler, A. Lueschow, G. Curio, and L. Trahms, "Cardiac artifact subspace identification and elimination in cognitive MEG data using time-delayed decorrelation," *IEEE Trans. Biomed. Eng.*, vol. 49, pp. 345–354, Apr. 2002.

Kensuke Sekihara received the M.S. degree and Ph.D. degrees from Tokyo Institute of Technology, Tokyo, Japan, in 1976 and 1987, respectively.

From 1976 to 2000, he worked with Central Research Laboratory, Hitachi, Ltd., Tokyo. He was a visiting Research Scientist at Stanford University, Stanford, CA, from 1985 to 1986, and at Basic Development, Siemens Medical Engineering, Erlangen, Germany, from 1991 to 1992. From 1996 to 2000, he worked with the "Mind Articulation" research project sponsored by Japan Science and Technology Corporation. He is currently a Professor at the Tokyo Metropolitan Institute of Technology. His research interests include the neuromagnetic source reconstruction, and statistical signal processing, especially its application to functional neuroimaging.

Dr. Sekihara is a member of IEEE Medicine and Biology Society and the IEEE Signal Processing Society.

Srikantan S. Nagarajan received the B.S. degree in electrical engineering from the University of Madras, Madras, India, and the M.S. and Ph.D. degrees from the Department of Biomedical Engineering at Case Western Reserve University, Cleveland, OH, in 1993 and 1995 respectively.

From 1995–1998, he was a Postdoctoral Fellow at the Keck Center for Integrative Neuroscience, the University of California, San Francisco (UCSF). In 1999, he was a full-time Research Scientist at Scientific Learning Corporation, Berkeley, CA, and an Adjunct Assistant Professor in the Department of Otolaryngology at UCSF. From 2000–2002, he was an Assistant Professor in the Department of Bioengineering at the University of Utah, Salt Lake City. Currently, he is the Director of the Biomagnetic Imaging Laboratory and an Assistant Professor in Residence in the Department of Radiology at UCSF. His research interests in neural engineering include multimodal and multiscale functional brain imaging using fMRI, MEG, EEG, systems and computational neuroscience, neuro-rehabilitation.

David Poeppel received the B.S. and Ph.D degrees in cognitive neuroscience from the Massachusetts Institute of Technology, Cambridge, in 1990 and 1995 respectively.

He is currently an Associate Professor in the Departments of Linguistics and Biology at the University of Maryland at College Park. His research uses the functional neuroimaging methods magnetoencephalography (MEG), electroencephalography (EEG), positron emission tomography (PET), and functional magnetic resonance imaging (fMRI) to investigate the neural basis of speech and language processing.

Alec Marantz received the B.A. degree in psycholinguistics from Oberlin College, Oberlin, OH, in 1978 and the Ph.D. degree in linguistics from the Massachusetts Institute of Technology (M.I.T.), Cambridge, in 1981. He joined the faculty at M.I.T. in 1990, where he is currently the Kenan Sahin distinguished Professor of Linguistics and Head of the Department of Linguistics and Philosophy. His research interests include the syntax and morphology of natural languages, linguistic universals, and the neurobiology of language. He is currently involved in revising morphological theory within linguistics and in exploring MEG techniques to uncover how the brain processes language.